JOURNAL OF SPACECRAFT AND ROCKETS
Vol. 59, No. 4, July–August 2022

Constrained Guidance for Spacecraft Proximity Operations Under Electrostatic Perturbations

Kieran Wilson,* Álvaro Romero-Calvo,* and Hanspeter Schaub†
University of Colorado Boulder, Boulder, Colorado 80301

https://doi.org/10.2514/1.A35162

Electrostatic perturbations can have significant effects during terminal proximity operations in high Earth orbits, with torque levels exceeding 5 $\mathrm{mN \cdot m}$ during severe charging events. These torques can impart $1^\circ/\mathrm{s}$ rotational rates to uncontrolled bodies, such as debris or servicing clients, during rendezvous and proximity operations. A suboptimal, but deterministic and computationally efficient, sampling-based method is presented here to minimize the impact of these torques during rendezvous, combining prior innovations in rapidly computing the electrostatic torque between bodies and in determining the electrostatic potential on objects remotely. This method is applied to a simulated servicing scenario, and found to reduce the accumulated rotational rates of the target by over 50%, yielding significant improvements in control effort, and potential improvements in safety. This iterative method is compared to an optimized strategy to minimize final rotational rate of a target, using a pseudospectral collocation-based approach. The globally optimized approach requires a priori knowledge of both spacecraft potentials throughout the approach, which limits its applicability in practice, but was found to be robust to moderate misestimates in potentials.

Nomenclature

$\boldsymbol{A}$ = area of surface
$\boldsymbol{B}$ = magnetic flux density, T
C = capacitance, F
$\boldsymbol{E}$ = electric field, V/m
$\boldsymbol{e}$ = construction vector
$\boldsymbol{F}$ = force vector, N
$[I]$ = inertia matrix, $\mathrm{kg \cdot m^2}$
$\mathcal{J}$ = cost function
$[K]$ = control gain matrix
k_c = Coulomb's constant, $\approx 8.99 \times 10^9\ \mathrm{Nm^2/C^2}$
$\boldsymbol{L}$ = torque vector, $\mathrm{N \cdot m}$
$[M]$ = fitting coefficients matrix
n = number of spheres
$\boldsymbol{n}$ = face normal vector
P_{SRP} = solar radiation pressure, $\mathrm{N/m^2}$
$\boldsymbol{Q}$ = charge vector, C
q = charge, C
r = distance between spheres, m
$\boldsymbol{r}$ = position vector, m
R = radius of sphere, m
$[S]$ = Elastance matrix, $\mathrm{F^{-1}}$
$\hat{\boldsymbol{S}}$ = sun vector
$\boldsymbol{s}$ = line of sight vector
t = time, s
$\boldsymbol{u}$ = control input, $\mathrm{m/s^2}$
V = electrostatic potential, V
$\boldsymbol{v}$ = velocity vector, m/s
$\mathcal{V}$ = Lyapunov function
$\{x, y, z\}$ = Cartesian frame, m
$\boldsymbol{\beta}$ = quaternion
β_D = diffuse reflection coefficient
β_s = specular reflection coefficient
ΔV = relative potential, V
$\boldsymbol{\epsilon}$ = vector components of quaternion error
ϵ_0 = vacuum permittivity, $\approx 8.854 \times 10^{-12}$ F/m
θ = angle between $\hat{\boldsymbol{n}}$ and $\hat{\boldsymbol{s}}$, rad
$\boldsymbol{\kappa}$ = state vector for trajectory
$\boldsymbol{\rho}$ = error vector in position, m
ϕ = sensor-target angle, rad
χ = dimensionless x coordinate
ψ = spacecraft rotation angle
$\boldsymbol{\omega}$ = angular velocity vector, rad/s
$\times$ = cross product
$\cdot$ = scalar product
$\dot{W}$ = time derivative
$\ddot{W}$ = double time derivative
W' = target-frame time derivative
W'' = double target-frame time derivative
dW/dW = total derivative
$\hat{W}$ = unit vector
$[\tilde{W}]$ = Skew-symmetric matrix

Subscripts

ext = external disturbance
f = final time
i = body i
i, j = i relative to j
n = orbital mean motion
S = servicer
T = target
0 = initial time

Superscripts

$\mathcal{H}$ = Hill frame
$\mathcal{S}$ = servicer frame
$\mathcal{T}$ = target frame
T = transpose
$*$ = reference trajectory

I. Introduction

RECENT work has demonstrated the potential dynamic impact of electrostatic perturbations on proximity operations, particularly in high Earth and geostationary orbital regimes where high spacecraft potentials may be encountered [1,2]. Spacecraft in the region, for instance, can charge to tens of kilovolts depending on local space

---

Received 11 May 2021; revision received 27 January 2022; accepted for publication 30 January 2022; published online 22 March 2022.

*Graduate Research Assistant, Ann and H. J. Smead Aerospace Engineering Sciences Department. Member AIAA.

†Glenn L. Murphy Endowed Chair, Ann and H. J. Smead Aerospace Engineering Sciences Department. Fellow Member AIAA.

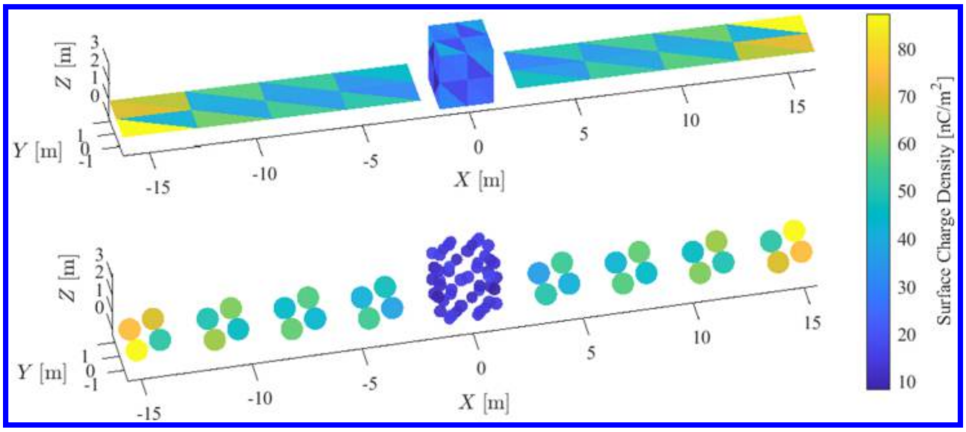

Fig. 1 Example of a spacecraft model discretized into 84 elements for use in the Method of Moments finite element formulation (top), and the equivalent multisphere model (bottom).

weather conditions [3]. While such charging events are relatively infrequent, proximity operations during these times are significantly perturbed by the electrostatic forces and torques acting between the spacecraft; cases with an uncontrolled target body, such as a servicing or debris remediation mission, are particularly affected [2]. With the increasing popularity and necessity of such missions in high Earth orbits, there is a need to consider these induced dynamic effects, which can impart target tumble rates exceeding a degree per second to an uncontrolled target during rendezvous [2]. Such rotational rates significantly complicate rendezvous, imposing high propellant usage demands on the servicer and posing a much more challenging navigation scenario than rendezvous with a nonrotating target body, while increasing collision risk [2].

The system dynamics between two charged spacecraft are highly nonlinear, with mutual forces and torques dependent on the positions and attitudes of both spacecraft, as well as their geometries (which dictate charge distributions) and electrostatic potentials [4,5]. Two innovations make rapid guidance and control in these scenarios possible: the development of methods to accurately and remotely determine the potential on a co-orbiting object, and a method for rapidly evaluating the electrostatic forces and torques between nearby bodies. The electrostatic potential sensing method is based on observations of x-ray and electron spectra excited during energetic electron bombardment of the target, either in a controlled manner using an electron gun mounted to the servicer, or by relying on hot electrons present in the ambient plasma environment [6]. Force and torque computations are then performed using the multisphere method (MSM), a computationally efficient means of approximating the electric fields around a body to within a few percent, given knowledge of the target's geometry and electrostatic potential [5].

The goal of this work is to combine these innovations in a guidance and control framework to meet proximity operation goals while minimizing the impact of electrostatic perturbations, in positional errors, fuel consumption, or tumble rates imparted to the target. Combining touchless potential sensing and MSM allows for rapid evaluation of the anticipated forces and torques, suitable for implementation aboard flight hardware. This work enables safer, more robust proximity operations during periods of heightened electrostatic charging, which in turn can enable expanded opportunities for engaging in proximity operations.

This paper is organized as follows. First, the system dynamics are established, consisting of translational and rotational dynamics. Perturbing forces and torques created by electrostatic interactions are introduced, along with methods for rapidly evaluating the force and torque contributions, and the relative magnitudes of each compared to those exerted by solar radiation pressure. Two methods for evaluating the electrostatic potential of an object remotely are provided in review. A guidance strategy is then introduced enabling rapid computation of a torque-minimal approach to an inert target object. This strategy is numerically simulated, and performance contrasted to an approach that does not account for electrostatic perturbations. This creates a near-optimal approach trajectory while maintaining operational constraints on approach angles. As a counter point to this iterative approach, a globally optimized trajectory for the same scenario is developed. The optimal trajectory is based on pseudospectral collocation and optimized to minimize final rotational rate of the target rather than the net torque at each time step, but requires foreknowledge of the spacecraft charge state throughout the approach.

II. Problem Scenario

The scenario relevant to this work involves a servicer approaching an inert target spacecraft, where both spacecraft have accumulated significant electrostatic potentials as a result of interactions with the space environment. While significant multi-kilovolt level charging events at geostationary orbit are relatively rare, occurring perhaps a few days per year on average, they occur more frequently during periods of heightened solar activity [7]. Additionally, some components of spacecraft and debris objects may not be continuously conducting with the spacecraft frame, and may be composed of dielectric or other materials that experience charging differently than conducting metal structures. These components may be subject to significantly higher levels of charging than a fully conducting spacecraft structure, with data from the ATS-6 mission showing a Kapton element at a floating potential having over 100× the electrostatic potential of the spacecraft frame [8]. Modern spacecraft construction guidelines are formulated to avoid differential spacecraft potentials and typically discourage the use of external dielectrics in orbits subject to high charging conditions like GEO [9,10]. However, many spacecraft currently in orbit were launched before the development of these guidelines, and spacecraft on orbit can experience material degradation that impacts the efficacy of mitigation strategies [11]. Additionally, even with adherence to these guidelines numerical simulations show that modern spacecraft can exceed kilovolt potential levels under severe plasma conditions at GEO in sunlight [12], and observations have shown that operational GEO satellites continue to experience arcing events indicative of high levels of spacecraft charging [13]. While such events are believed to be infrequent, they are more common during solar maximum periods, with highly perturbed K_p index measurements accounting for over 15% of measurements in some historical periods near solar maximum [14,15].

Additionally, other work has shown that the use of spacecraft charging models to estimate the electrostatic potential on an object based on space weather conditions can dramatically misestimate the true potential of the spacecraft, so it is important not to simply assume a potential on a target body, but actively monitor the potential during proximity operations [16,17].

III. Dynamics

A. Electrostatic Force and Torque Computation

Standard methods for computing the electrostatic forces and torques between bodies rely on finite element analyses [18]. These techniques are typically highly accurate, but require significant computational resources that make them impractical for modeling system dynamics. However, the recently developed MSM enables rapid evaluation of the electrostatic interactions between bodies to within a few percent accuracy, and at a fraction of the computational cost [5,19]. This method discretizes an object as a series of spheres, with the sphere positions and radii tuned to match a parameter of the object (typically the object's self-capacitance). A straightforward method to choose sphere radii is to match the capacitance of the sphere to a corresponding finite element; the sphere is located at the element centroid in the heterogeneous surface MSM development [5]. Analytic expressions for the mutual capacitance effects of multiple spheres are used to determine the charge on each sphere q_i for a given voltage V_i. The simplest example is the case of two nearby spheres, which is represented as

$$\begin{bmatrix} q_1 \\ q_2 \end{bmatrix} = \underbrace{\frac{r}{k_c(r^2 - R_1 R_2)} \begin{bmatrix} rR_1 & -R_1 R_2 \\ -R_1 R_2 & rR_2 \end{bmatrix}}_{C_V} \begin{bmatrix} V_1 \\ V_2 \end{bmatrix} \tag{1}$$

where R_1 and R_2 are the sphere radii, and r represents the L2 norm distance between the spheres. Equation (1) expanded to an $n \times m$ matrix, where the first object is composed of n spheres and the second of m spheres, as seen in Eq. (2).

$$\begin{pmatrix} V_1 \\ V_2 \\ \vdots \\ V_n \end{pmatrix} = k_c \begin{bmatrix} 1/R_1 & 1/r_{1,2} & \cdots & 1/r_{1,n} \\ 1/r_{2,1} & 1/R_2 & \cdots & 2/r_{2,n} \\ \vdots & \vdots & \ddots & \vdots \\ 1/r_{n,1} & 1/r_{n,2} & \cdots & 1/R_n \end{bmatrix} \begin{pmatrix} Q_1 \\ Q_2 \\ \vdots \\ Q_n \end{pmatrix} \tag{2}$$

Equation (2) is expressed as the simple relation relating the charge $\boldsymbol{Q}$ and potential $\boldsymbol{V}$:

$$\boldsymbol{V} = [S]\boldsymbol{Q} \tag{3}$$

where $[S]$ is the elastance matrix, which is the inverse of the capacitance matrix C_v. Therefore, if the voltages, positions, and radii of each sphere are known, then the charge on each is computed by inverting Eq. (3).

Once the charge on each sphere is known, then the forces and torques between each body are evaluated. The force contributions of each charge in body 2 (q_j) acting on each charge in body 1 (q_i) is evaluated as

$$\boldsymbol{F} = k_c \sum_{j=1}^{n_1} q_j \left(\sum_{i=1}^{n_2} \frac{q_i}{r_{i,k}^3} \boldsymbol{r}_{i,j} \right) \tag{4}$$

The resultant torque about the center of mass $\boldsymbol{L}_o$ is then given as

$$\boldsymbol{L}_o = k_c \sum_{j=1}^{n_1} q_j \left(\sum_{i=1}^{n_2} \frac{q_i}{r_{i,j}^3} \boldsymbol{r}_i \times \boldsymbol{r}_{i,j} \right) \tag{5}$$

It is important to note that r_i is the distance from a sphere in the body of interest to the center of mass of that body, while $r_{i,j}$ represents the distance from sphere i in body 1 to sphere j in body 2.

While computationally efficient, the MSM formulation still requires initialization using a finite element analysis. This analysis provides a truth capacitance used to tune each sphere position and radius to accurately capture the charge distribution across the surface. The method of moments (MoM) is used here, as seen in Fig. 1 and described in detail by Ref. [5]. For comparison, a high-fidelity MoM finite element setup with two 500-element spacecraft required approximately 1000 s of computation time to find the forces and torques acting between the bodies. The equivalent-fidelity MSM model required less than 0.2 s, for a 10^4 speed up; lower-fidelity MSM models are evaluated faster still with minimal loss of accuracy [5]. The finite element truth model only needs to be computed once for a structure, and the resulting MSM model is then valid for any future case, including with flexible or time-varying structures, or multiple spacecraft operating in close proximity [20]. This makes MSM ideally suited for faster-than-realtime dynamics propagation, or real-time guidance.

Rigid bodies are assumed for the MSM structures here. However, the MSM formulation extends readily to time-varying geometries, such as servicer solar arrays rotating to track the sun or extending robotic arms [20]. These time-varying structures can be solved without requiring an update of the computationally intensive finite element computation step, but can instead be updated using only the MSM formulation.

B. Sensing Electrostatic Potentials Remotely

The electrostatic potential of each object must be known to effectively utilize the MSM for computation electrostatic forces and torques. Numerical modeling is often insufficient for accurately characterizing the electrostatic potential of spacecraft, due to large uncertainties in material properties [11,21]. Therefore, it is essential to perform actual measurements of spacecraft potentials in situ, both of a spacecraft's own potential and the potential of the target body.

Several flight-proven techniques exist to determine the electrostatic potential of a spacecraft equipped with requisite instruments, as a servicer would be assumed to carry. One approach utilizes deployable booms with electric field instruments, which can extend into the surrounding plasma to determine the potential of the spacecraft relative to a point tens of meters away [22]. An alternative technique uses an ion energy spectrometer to observe a stable reference line present in the ion population of the plasma environment. As the spacecraft potential changes, the observed energy of the known reference population changes, determining the spacecraft potential relative to the plasma. As space plasmas are typically regarded as neutral, these methods for spacecraft self-potential monitoring provide an absolute estimate of the quantity of excess charge on an object [23].

While methods to assess the potential of an instrumented spacecraft relative to the surrounding plasma have been well established for decades, only recently have two methods been developed to determine the electrostatic potential of an un-instrumented object without requiring physical contact. Reference [15] describes a technique to estimate the potential of a target to within ~100 V using bremsstrahlung x-rays emitted by the interactions of energetic electrons with the target. The energetic electrons could either come from an electron gun on the servicer, or the ambient plasma in high Earth orbit [24]. The second technique is covered in Ref. [25], and involves measuring the electrons emitted from the target through either solar-induced photoemission, or secondary electrons generated by incident energetic electrons in the ambient plasma or from an electron beam. The electron-based method can resolve target potentials with an accuracy of ~10 V. However, the electron-based method has far lower observability of the target potential, with a useful signal available for only ~10% of a revolution of a tumbling target body [6]. By contrast, the bremsstrahlung-based method showed signal availability in over 70% of a target rotation [6].

These two methods can be used in tandem to provide an accurate estimate of the target's electrostatic potential, with the bremsstrahlung-based method enabling a relatively low-resolution estimate with high levels of observability, while the electron-based method enables high-resolution measurements with low availability. An adaptive Kalman filter is used in Ref. [6] to fuse the measurements of each method into a single estimate of the relative potential between the spacecraft, with a typical accuracy on the order of 10 V.

A relevant concern is whether such accuracy is sufficient for effective modeling of intercraft forces and torques. A first-order sensitivity analysis is introduced here to evaluate the required potential sensing accuracy, as well as sensitivity of the computed forces and torques to ranging and attitude estimation.

C. Dynamic Sensitivity to Estimated Potential and Range

The following analysis covers a two-craft rendezvous scenario in a geostationary graveyard orbit. It includes electrostatic perturbations, and solar radiation pressure (SRP) is also modeled as the other dominant perturbation in the GEO regime. The high-altitude orbital regimes that are most susceptible to prolonged, high-intensity electrostatic charging have negligible drag, so this disturbance is omitted [26]. A few fundamental assumptions underpin the use of MSM here. First, the sphere radii and positions are derived from a finite element model (FEM) of each spacecraft, taken as a ground truth. This truth model requires accurate representations of the surface geometry of both spacecraft; through a combination of a priori knowledge of the target and systems like LiDAR, this is readily achievable [27]. Next, the relative position and attitude of the spacecraft must be known to accurately compute the relative positions of each pair of spheres. Relative pose estimation remains an area of active research, but it is possible to obtain pose estimates of an uncooperative target with less than a degree of error using modern 3D flash LiDARs, stereo cameras, or other techniques [28].

The electrostatic force $F^e_{S,T}$ between charged bodies is computed through MSM, and torque is then computed as the cross product between the electrostatic force vector and the radius from the point of force application to the body center of mass. Torque computation therefore requires an accurate evaluation of the target body's center of mass. Furthermore, to predict the resultant rotational dynamics an accurate estimate of the target's inertia matrix is needed. For a cooperative servicing target these values should be well-documented, even in an end-of-life scenario. However, for a debris object these parameters may require estimation on-orbit by observing the rotational properties of the target. If the shape and potential of the target are known it is possible to use electrostatic interactions and proximity flight to deliberately introduce perturbing torques to the target. The target's resulting rotational behavior can then be used to estimate its inertia parameters. The ability to apply a known external torque to a body may enable improvements in performance over previously proposed methods to estimate the inertia properties of tumbling bodies like those described by Ref. [29].

Finally, the electrostatic potential of both the servicer and target must be known. The methods for remote potential sensing can achieve consistent target voltage estimates within 100 V or less [15]. However, no work has yet been conducted to evaluate the potential estimation accuracy required for sufficiently accurate dynamic evaluations. In related work, Ref. [4] explores the impact of erroneous total system charge product (the product of multiplying the charges on each spacecraft) on the closed-loop control stability characteristics of an actively charged electrostatic tractor debris tugging scenario. The authors find that the closed loop control can bifurcate and become unstable if charge is misestimated by just 40%, making it critical that an accurate measure of electrostatic potentials be available.

While the electrostatic potential may be sensed remotely, electrostatic charges are responsible for producing force and torque interactions between the bodies. The charge is related to the potential on a body by the body's capacitance, which is chiefly determined by the body's surface geometry.

A reduced-order analysis is developed to evaluate the sensitivity of the computed force and torque to the estimated electrostatic potential and intercraft distance. To gain analytic insight into the sensitivity, each body is modeled as a single sphere, as seen in Fig. 2. This is the simplest configuration that still includes mutual capacitance effects. An S subscript denotes a property of the servicer and a T the target. The force acting between the spheres is then found as

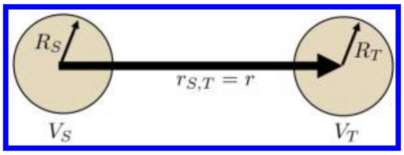

Fig. 2 Illustration of two-sphere system evaluated.

$$F = \frac{k_c q_S q_T}{r^2} \tag{6}$$

where k_c is Coulomb's constant, q_S is the charge on the servicer, q_T is the target charge, and r is the distance between the spheres.

Therefore, electrostatic charges on each sphere are calculated as a function of their potentials, computed as in Eq. (2). The upper-right and lower-left elements of the capacitance matrix represent mutual capacitance effects, caused by the interactions of the two bodies. These elements are expanded as

$$q_S = \frac{r}{k_c(r^2 - R_S R_T)}(r R_S V_S - R_S R_T V_T) \tag{7}$$

$$q_T = \frac{r}{k_c(r^2 - R_S R_T)}(r R_T V_T - R_S R_T V_S) \tag{8}$$

Combining this expansion with Eq. (6) yields a force expression as

$$F = \left[\frac{r}{k_c(r^2 - R_S R_T)}\right]^2 [(r^2 + R_S R_T) V_S V_T \quad - r R_S V_T^2 - r R_T V_T^2] \tag{9}$$

where the leading term is constant with respect to voltage. However, in practice, the measured quantities are the potential of the servicer V_S and the relative potential of the target relative to the servicer $\Delta V_{T,S}$. Therefore

$$V_T = V_S + \Delta V_{T,S} \tag{10}$$

The force between the bodies then becomes

$$\begin{aligned} F = \left[\frac{r}{k_c(r^2 - R_S R_T)}\right]^2 [&(r^2 + R_S R_T) V_S (V_S + \Delta V_{T,S}) \\ &- r R_S (V_S + \Delta V_{T,S})^2 - r R_T (V_S + \Delta V_{T,S})^2] \end{aligned} \tag{11}$$

Typically, the effects of electrostatic interactions only become significant for cases where potentials exceed a few kilovolts. In this range, the typical 1σ uncertainty in the measurements are in the region of <1–10%. For a case with a 10% error in the relative potential estimate between the spacecraft, the resultant force estimation error is only about 8%, as seen in Fig. 3, on the same order as the errors associated with the MSM formulation.

Common methods for measuring a spacecraft's own potential relative to the ambient plasma are limited in accuracy by the energy resolution of the instruments used, but can typically resolve spacecraft potentials to within <5% [23]. Because the remote potential sensing methods here provide only relative potentials, the net error in a target's absolute potential will be a combination of errors in both the relative potential and a spacecraft's self-potential measurement.

The sensitivity of force to error in either the voltage of the servicer (V_S) or the potential of the target relative to the servicer ($\Delta V_{T,S}$) can be evaluated by taking the ratio of the partial derivatives of the electrostatic force with respect to V_S and $\Delta V_{T,S}$. The resultant ratio, seen in Eq. (13), is a function of not just V_S, $\Delta V_{T,S}$ but also of the problem geometry (sphere radii and separation distance). The ratio of

$$\frac{\partial F / \partial V_S}{\partial F / \partial \Delta V_{T,S}} \tag{12}$$

is independent of the base voltage of each sphere; the ratio remains the same regardless of V_S and V_T as long as $V_S = V_T$.

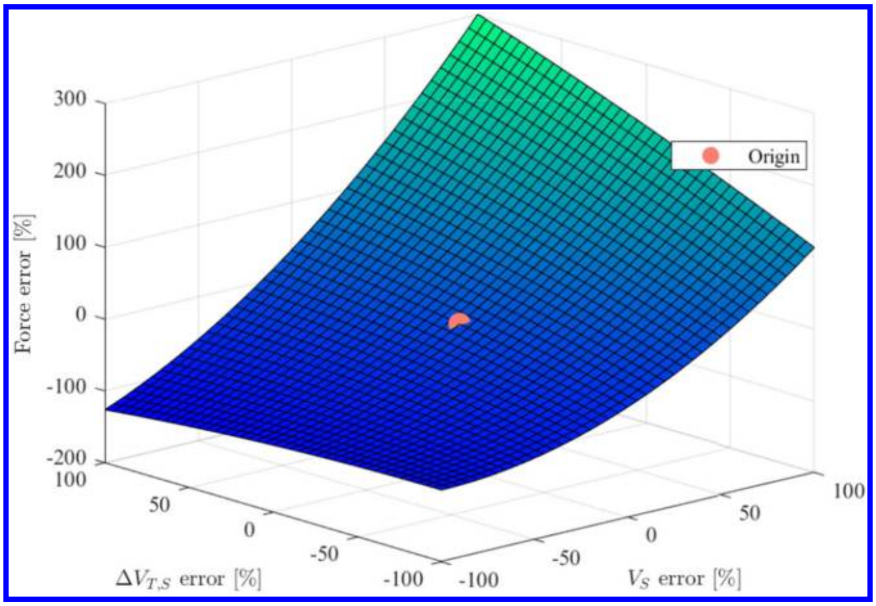

Fig. 3 Sensitivity of electrostatic force to errors in $\Delta V_{T,S}$ and V_S.

$$\frac{\partial F/\partial V_S}{\partial F/\partial \Delta V_{T,S}} = \frac{(2V_S + \Delta V_{T,S})(r^2 + R_S R_T) - 2R_S V_S r - 2R_T r(V_S + \Delta V_{T,S})}{V_S(r^2 + R_S R_T) - 2R_T r(V_S + \Delta V_{T,S})} \tag{13}$$

Ultimately, the system is far more sensitive to V_S than $\Delta V_{T,S}$. The exact value of the sensitivity ratio is a function of both voltages and the positions of each sphere, but is typically somewhere between 3 and 10 for most combinations of potentials from 1 to 20 kV and positions from 1 to 20 m. Potentials on both spacecraft should be similar if they are exposed to near-identical space environment conditions, but differences in construction and material properties may result in significant, multi-kilovolt-level differences [8]. For a nominal case where each spacecraft is charged to 10 kV at 10 m separation, Fig. 3 illustrates the relationship between misestimated potentials on each sphere and the resultant force. As expected, the force error is significantly more affected by errors in V_S than V_T, with the relation nearly linear in the region of <10% errors. Nonlinearities in this relation become more pronounced as errors exceed 20%, but it is reasonable that this figure should account for most potential measurement uncertainties using existing techniques.

Given the relatively high electrostatic potentials of interest in this problem, it is worth considering the dynamic effects of charged spacecraft interactions with the environment. Two interactions are considered: the effect of the charged spacecraft's interactions with Earth's magnetic field (Lorentz force) and ionospheric drag, due to the interaction of a charged spacecraft with ambient charged particles. The total charge on a spacecraft charged to a near-record −20 kV is approximately 1×10^{-5} C. The Lorentz force can then be computed as

$$\boldsymbol{F} = q(\boldsymbol{E} + \boldsymbol{v} \times \boldsymbol{B}) \tag{14}$$

which, given a nominal GEO magnetic field intensity of 106 nT [30], orbital velocity $v = 3$ km/s, and electric field intensity on the order of 1 mV/m [31], the Lorentz force can be estimated to be on the order of 10^{-8} N—approximately 1/3 the gravitational force exerted by the moon, and 5–6 orders of magnitude smaller than intercraft electrostatic forces.

Likewise, plasma densities at GEO are often very low compared to LEO orbits, with typical plasma densities on the order of 10^5 ions per cubic meter [32] compared to some five orders of magnitude greater in LEO at 500 km. These low plasma densities, combined with low orbital velocities, result in negligible ionospheric drag forces.

Table 1 Solar radiation pressure reflectance parameters from [33]

Material	β_s	β_D
Multilayer insulation (spacecraft bus)	0.29	0.29
Black paint (solar array rear)	0.015	0.015
Solar array front	0.073	0.007

While the contributions of Lorentz forces and ionospheric drag are negligible, the dominant perturbation at high Earth orbits is typically SRP [33], which can affect a spacecraft's inertial acceleration and also impart significant torques. The first-order SRP model used here divides each spacecraft into a series of rectangular elements, representing a face of a solar array or a side of a bus. Each element is subject to the force

$$\boldsymbol{F}_i = -P_{\text{SRP}}\Big((1 - \beta_{s,i})\hat{\boldsymbol{s}} + 2\Big(\beta_{s,i}\cos(\theta_i) + \frac{1}{3}\beta_{D,i}\Big)\hat{\boldsymbol{n}}_i\Big) \cdot \cos(\theta_i)A_i \tag{15}$$

Here, β_s represents the specular reflection coefficient, and β_D is the diffuse reflection coefficient for the given element. Values used are provided in Table 1. The sun direction unit vector is given by $\hat{\boldsymbol{s}}$, while $\hat{\boldsymbol{n}}_i$ is the face normal unit vector; θ_i describes the angle between $\hat{\boldsymbol{s}}$ and $\hat{\boldsymbol{n}}_i$. A_i is the area of the given element. Reflection and absorption coefficients for representative material surfaces were taken from Ref. [34].

IV. Control

A. System Frames

Three coordinate frames are used, as shown in Fig. 4. The Hill relative orbit frame $\mathcal{H}$ is assumed to be equivalent to an inertial frame for this scenario, and it originates at a virtual Keplerian chief. The target frame $\mathcal{T}$ is co-located and co-aligned with the Hill frame at the beginning of the simulation. The target frame is fixed to the docking port on the target body. The servicer frame $\mathcal{S}$ is fixed to the servicer docking port.

The reference trajectory is given by ${}^{\mathcal{T}}\boldsymbol{r}^* = [x^*, y^*, z^*]^T$, and right star superscripts are used to denote reference quantities. The reference is computed in the target-fixed frame, which aligns with a Hill-frame approach if no perturbations are present. However, if the target is rotating, the servicer will need maneuver in the Hill frame to track the reference trajectory in $\mathcal{T}$.

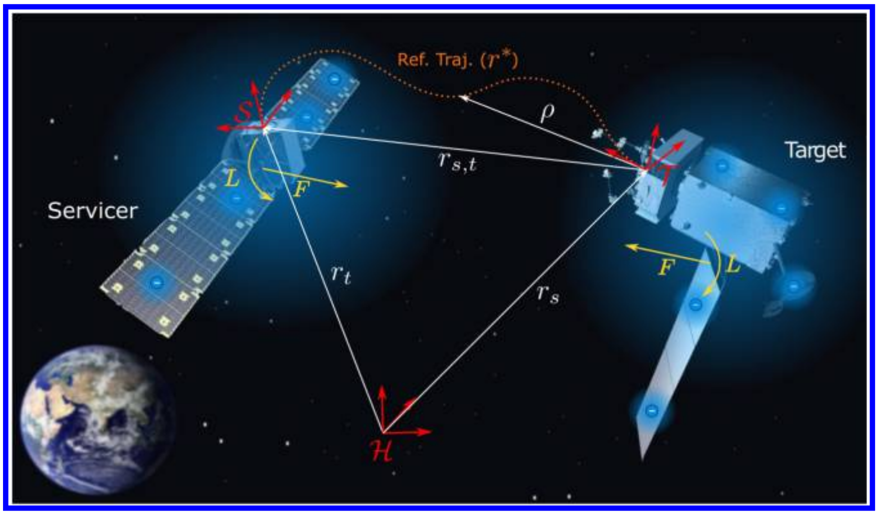

Fig. 4 Illustration of electrostatic interactions between two proximate spacecraft. The reference frames are depicted, with $\mathcal{H}$ being the Hill frame, taken to be inertial for this scenario; $\mathcal{S}$ the frame fixed to the servicer; and $\mathcal{T}$ the one fixed to the target's docking port.

B. Translational Control

The goal of the control system is to track the reference trajectory by driving the position and velocity errors to zero. Error terms are given by

$$\boldsymbol{\rho} = \boldsymbol{r}_{S/T} - \boldsymbol{r}^*_{S/T} \tag{16}$$

$$\dot{\boldsymbol{\rho}} = \dot{\boldsymbol{r}}_{S/T} - \dot{\boldsymbol{r}}^*_{S/T} \tag{17}$$

as seen in Fig. 4.

The system dynamics are inherently nonlinear due to the coupling of position, attitude, and resultant force and torque. Therefore, a nonlinear Lyapunov-derived Cartesian feedback controller is implemented to track the desired reference trajectory computed by the guidance system [35]. The positive definite Lyapunov candidate function is chosen to be

$$\mathcal{V}(\boldsymbol{\rho},\dot{\boldsymbol{\rho}}) = 1/2[K_1]\boldsymbol{\rho}^T\rho + 1/2\dot{\boldsymbol{\rho}}^T\dot{\boldsymbol{\rho}} \tag{18}$$

The derivative of $\mathcal{V}(\boldsymbol{\rho},\dot{\boldsymbol{\rho}})$ is then

$$\dot{\mathcal{V}}(\boldsymbol{\rho},\dot{\boldsymbol{\rho}}) = \dot{\boldsymbol{\rho}}^T(\boldsymbol{u}_s + (\ddot{\boldsymbol{r}}_{S,T} - \ddot{\boldsymbol{r}}^*_{S,T}) + [K_1]\boldsymbol{\rho}) \tag{19}$$

which takes the negative semidefinite form

$$\dot{\mathcal{V}}(\boldsymbol{\rho},\dot{\boldsymbol{\rho}}) = -\dot{\boldsymbol{\rho}}^T[K_2]\dot{\boldsymbol{\rho}} \tag{20}$$

for the control input

$$\boldsymbol{u}_s = -(\ddot{\boldsymbol{r}}_{S,T} - \ddot{\boldsymbol{r}}^*_{S,T}) - [K_1]\boldsymbol{\rho} - [K_2]\dot{\boldsymbol{\rho}} \tag{21}$$

and positive definite matrices for the control gains $[K_1]$, $[K_2]$. Here the term $(\ddot{\boldsymbol{r}}_{S,T} - \ddot{\boldsymbol{r}}^*_{S,T})$ represents the relative Hill-frame acceleration between the reference in $\mathcal{T}$ and $\mathcal{H}$ as a result of differential gravitational accelerations and the rotation of the target body with respect to $\mathcal{H}$. It is assumed that the target body's rotational rates and pose are known, likely through a combination of image-based and LiDAR-based methods. By feeding forward on these known relative accelerations, the servicer achieves better tracking and convergence at lower control effort cost.

As the target body rotates with angular velocity $\boldsymbol{\omega}_{T/H}$, the reference position will accelerate relative to the Hill frame. The Hill frame is assumed equivalent to an inertial reference frame. This acceleration is computed as

$$\ddot{\boldsymbol{r}}_{T/S} = r''_{T/S} + \dot{\boldsymbol{\omega}}_{T/H} \times \boldsymbol{r} + 2\boldsymbol{\omega}_{T/H} \times r'_{T/S} + \boldsymbol{\omega}_{T/H} \times (\boldsymbol{\omega}_{T/H} \times \boldsymbol{r}_{T/S}) \tag{22}$$

where the prime right superscript denotes a target-frame derivative, and dots a Hill-frame derivative [35].

The servicer spacecraft's 3-degree-of-freedom translation control is assumed to be independent, such that it can always command a Hill-frame acceleration to 0.01 $\mathrm{m/s^2}$.

C. Attitude Control

The attitude of the servicer must follow a time-varying reference to maintain a line-of-sight vector between the servicer's relative navigation sensors and the docking point on the target. The goal of the attitude controller is therefore to track the target's rotation such that the navigation system is always aligned to the docking port to avoid dropouts in navigation data. The attitude controller acts independently of the translation controller and, like the translation controller, has a maximum control effector limit but no minimum. This correlates well to an attitude control system reliant on momentum exchange devices like reaction wheels or control moment gyroscopes, while a reaction control system or other thruster-based method is used to apply translational control. The torque control limit is set to 100 $\mathrm{mN \cdot m}$, feasible for large reaction wheels like the Honeywell HR-12 series [36].

The attitude controller feeds back on the spacecraft attitude quaternion, and it is given by Ref. [35] as

$$\boldsymbol{T}_s = -K\boldsymbol{\epsilon}_{S/T} - P\delta\boldsymbol{\omega}_{S/T} + [I](\dot{\boldsymbol{\omega}}_{s^*} - [\tilde{\boldsymbol{\omega}}]\boldsymbol{\omega}_{s^*}) + [\tilde{\boldsymbol{\omega}}_{s^*}][I]\boldsymbol{\omega} - \boldsymbol{L}_{\text{ext}} \tag{23}$$

where the total external torque acting on the body $\boldsymbol{L}_{B,\text{ext}}$ is the product of the SRP and electrostatically induced torques

$$\boldsymbol{L}_{B,\text{ext}} = \boldsymbol{L}_{B,\text{SRP}} + \boldsymbol{L}_{B,\text{electro}} \tag{24}$$

and $\boldsymbol{\epsilon}_{S/T}$ is the three-element vector component of the quaternion attitude error $\boldsymbol{\beta}_{S/T}$.

$$\boldsymbol{\epsilon} = \boldsymbol{\beta}_{S/T}(1:3) = [\beta_1, \beta_2, \beta_3]^T \tag{25}$$

$\boldsymbol{T}_s$ is the control torque commanded by the servicer, and gains are $K = 0.01[I]_{3\times3}$ and $P = 0.001[I]_{3\times3}$. The inertia matrix used for numerical simulations is derived from a CAD model of the GOES-R spacecraft based on publicly available documentation, and it is taken to be

$$[I] = \begin{bmatrix} 15597 & -335 & 7070 \\ -335 & 23277 & -188 \\ 7070 & -188 & 23407 \end{bmatrix} \text{kg} - \text{m}^2 \tag{26}$$

This is not assumed to be an exact match to a specific operational vehicle, but instead to provide a reasonable estimate for the inertia matrix of a large GEO spacecraft.

V. Deterministic Guidance Approach

Prior studies into the topic of spacecraft proximity operations guidance under perturbations often focus on optimal control strategies to develop trajectories that minimize risk and fuel consumption [37]. These methods are typically computationally intensive, particularly when applied to systems with significant constraints and complex dynamics. Additionally, these methods may require reference trajectories to be computed a priori on the ground, while a controller or neighboring optimal solution follows the trajectory on board the spacecraft [37]. This is often problematic in the case of electrostatic perturbations, which vary significantly over a several-hour rendezvous process as spacecraft move through changing local plasma environments or lighting conditions. This results in dramatic changes in the relative motion dynamics between the two bodies, necessitating costly re-optimization [38].

It is very difficult to accurately predict the potential on a spacecraft, as this prediction is highly sensitive to space weather conditions and material properties. Therefore, global optimization of a multihour rendezvous requires some assumption of the environment. Alternatively, given the uncertain future system dynamics, the servicer could compute the optimal approach vector at that time step, and re-evaluate the desired approach as new measurements of target and servicer potential are available.

Both of these strategies, an iterative approach and a globally optimized approach, are developed here. The iterative approach that relies on a reduced-order MSM model is used to compute position and attitudes that most closely meet a desired torque, trading a small degree of accuracy for decreases in computational burden. The approach trajectory illustrated defines the servicer position and attitude relative to the target at each time step, providing 6-degree-of-freedom inputs to the controller. An alternative, globally optimized trajectory is also developed, using a polynomial-based pseudospectral collocation method. Rather than minimizing the imparted torque at each time step, this strategy computes an trajectory that minimizes the final rotational rate of the target.

A. Deterministic Translational Guidance

Several constraints are imposed on the approach trajectory. The nominal unperturbed trajectory is shown in Fig. 5 in the target frame $\mathcal{T}$. For a nonrotating target case, this corresponds to the Hill frame approach. The position and velocity for this approach are shown in Fig. 6. The trajectory is initialized at an 80 m range, a point where remote electrostatic potential measurements are expected to be available [6]. The servicer is required to perform three hold maneuvers at 10, 5, and 1 m from the docking point. The first two are set for 10 minutes, to allow ground controllers to verify navigation solutions or similar, while the final hold is commanded for 30 minutes to allow for robotic arms to perform grappling maneuvers. Hyperbolic tangent functions are used to smooth the approach trajectory to avoid acceleration singularities as seen in Fig. 6.

Repulsive electrostatic forces between the target and the servicer result in the target translating relative to the servicer and the servicer having to accelerate to pursue it. These accelerations are very small, on the order of 10^{-7} m/s^2. By comparison, torques generate rotational rates on the order of 0.1°/s, which correspondingly cause translational acceleration of the reference frame relative to the Hill frame. A servicer at 10 m distance must then chase with accelerations on the order of 10^{-4} m/s^2 or greater. Electrostatic torques are therefore a much more significant perturbation than electrostatic forces, and minimizing the impact of these torques on an inert target could

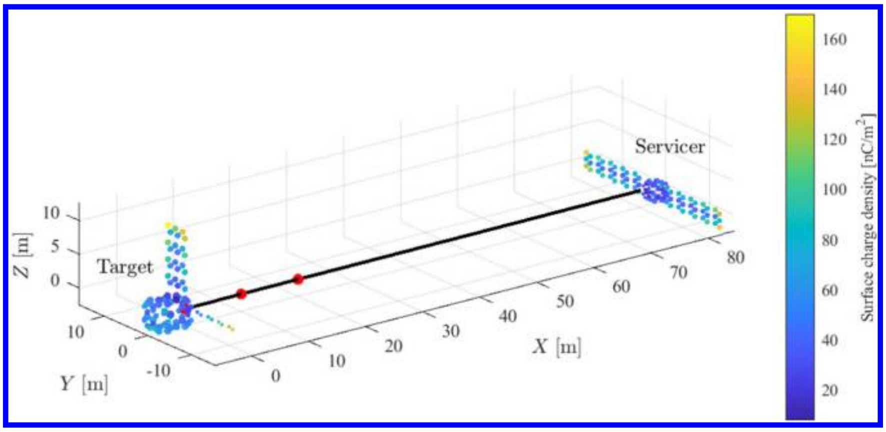

Fig. 5 The nominal approach trajectory from the two-panel servicer to the one panel target at the origin. Hold points are shown in red.

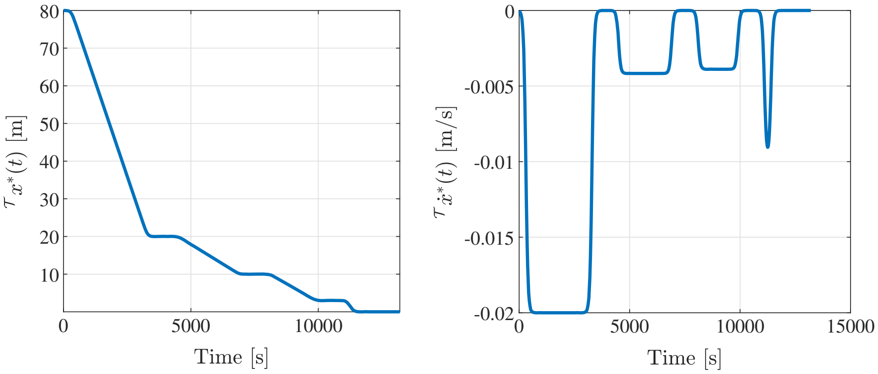

Fig. 6 Position and velocity of the target-frame desired rendezvous trajectory.

dramatically reduce the overall control effort required for proximity operation.

The final phase of autonomous rendezvous is highly dependent on an accurate navigation solution, typically obtained by a combination of LiDAR and visual or IR cameras. These impose line-of-sight constraints on the approach trajectory; not only does the servicer need to stay within a constraint cone of the docking point to allow satisfactory navigation sensor visibility, but the attitude of the servicer must also be constrained such that the RPO sensors have a direct line of sight to the docking location. For this work an approach cone with a 25° half angle is chosen, on a similar level to the approach angle observed in publicly available videos of the MEV-1 rendezvous operation. This approach cone is shown in Fig. 7. Despite being a relatively tight approach cone, there is significant variation in the magnitude and direction of electrostatic torques acting on the target in this area. Figure 8 illustrates an example of the torques imparted to a GOES-R target with a servicer at 10 m distance, and -10 kV on each spacecraft. Within the 25° approach cone there is a difference of over an order of magnitude between the lowest torque point (<0.2 mN · m) and the highest (>2.3 mN · m).

Due the relatively small region admissible under the constraints, a sampling-based strategy can efficiently evaluate the search space. The guidance strategy implemented here evaluates the electrostatic interactions between low-fidelity MSM models (20 sphere) of both spacecraft at 50 points over the 25° approach cone, with a fixed distance to the docking location as seen in Fig. 7. At each guidance update a new approach vector is computed based on the evaluation of the torque vector on the target, as seen in Fig. 9. The torque vector quantity acting on the target closest to a desired quantity is selected at each step. The servicer then follows a linear reference trajectory until the next guidance update.

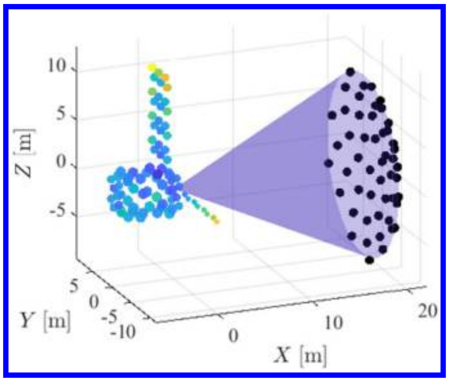

Fig. 7 Constraint cone fixed to target docking port, and selected test positions at a fixed distance to the target port.

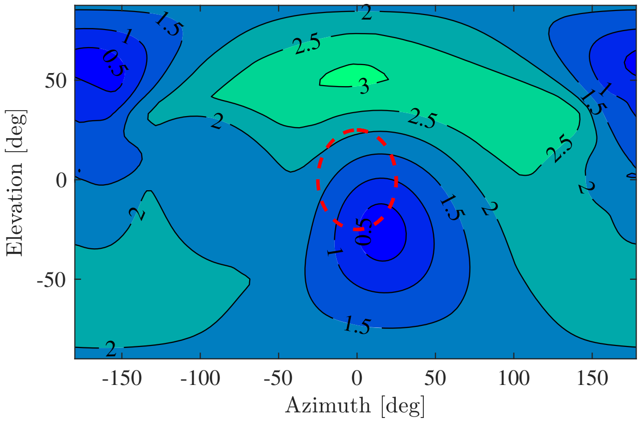

Fig. 8 Torque acting on a GOES-R target due to electrostatic interactions at a 10 m distance as a function of azimuth and elevation. Circled region corresponds to a 25° approach cone.

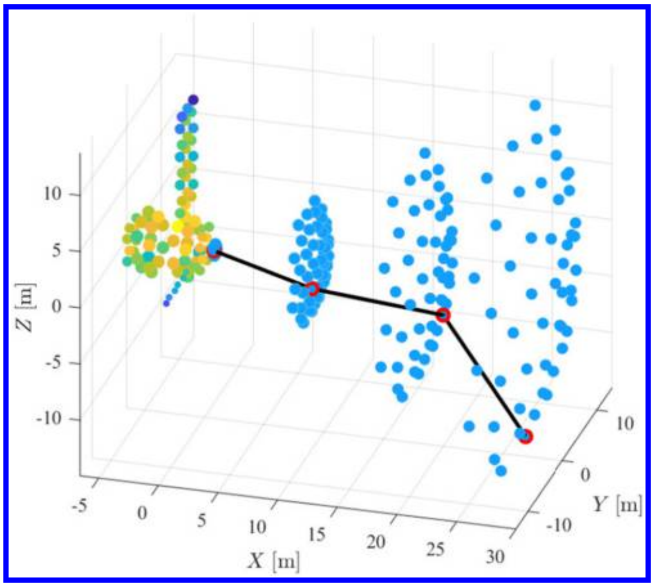

Fig. 9 Conceptual illustration of four updates of iterative guidance strategy. Best solution at each time step is shown in red; black line represents the servicer trajectory between each pair of points.

The position of each sample point is selected based on a spherical spiral to achieve near-evenly spaced points. The number of points to sample is chosen by evaluating the variation in electrostatic torques over the constraint cone, and then selecting a sample density that captures relatively small-scale variations in torque. In this case, the sensitivity of torque with respect to angle seen in Fig. 8 led to a 50-point sample, which ensures that the minimum torque is within 0.1 mN · m of the minimum sampled point for these spacecraft models. By constraining the distance to the target to be constant, this reduces to a constrained two-dimensional (in azimuth and elevation angle) search space, where the L_2 norm of the angles must be less than 25°.

The electrostatic forces and torques acting between the bodies are a function of the relative position of every sphere on each body, so both the target's attitude and position state need to be prescribed by the guidance algorithm at each time step. The RPO sensors must maintain a line of sight to the docking point, so the servicer must orient itself accordingly. However, this only constrains two degrees of rotational freedom for the servicer, which is free to rotate about the line of sight. As seen in Fig. 10, there are significant differences in torque as a servicer rotates through the one unconstrained degree of freedom. For this case, the maximum torque magnitude is over 20% higher than the minimum, which could have significant implications over a multihour proximity operation. Therefore, 50 attitudes are evaluated at each position, to find the combination of position and attitude that come closest to satisfying a desired torque as possible while maintaining a reasonable computational burden.

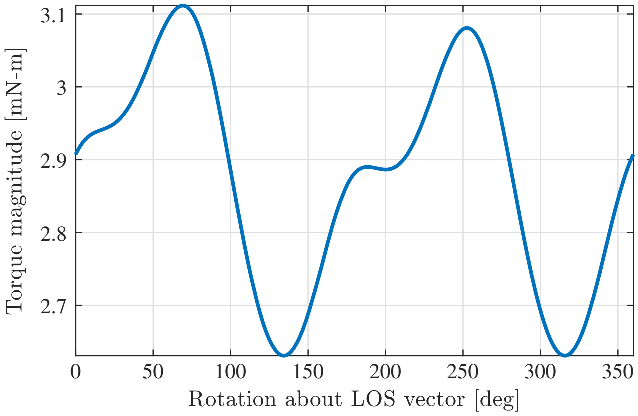

Fig. 10 Electrostatic torque imparted to the target as a function of servicer attitude, where the servicer is only rotated about the line of sight (LOS) vector.

Evaluating the intercraft forces and torques over 50 attitudes at 50 positions requires less than 0.1 s using MATLAB on a modern laptop computer. Using a higher-fidelity model with 4× more spheres per vehicle results in computation times increasing by a factor of 6×, with little change in the best position/attitude combination found.

The electrostatic potentials and intercraft forces will evolve over time periods on the order of minutes to tens of minutes, depending on separation distances and closure rates, so relatively slow updates of the guidance algorithm are acceptable for the system dynamics. The desired approach vector and attitude combination can be computed infrequently, making this solution well suited to implementation on board a servicing spacecraft. However, the MSM formulation tested here is sufficiently efficient that it could be implemented onboard a spacecraft with updates on the order of a second or less if desired.

B. Deterministic Attitude Guidance

The servicer attitude is prescribed to orient the sensors toward the docking point, computing the required quaternion between the sensor line of sight vector $\hat{s}$ and the relative $\mathcal{T}$-frame position of the servicer $\boldsymbol{r}_{S/T}$ as

$$\hat{\boldsymbol{e}} = \frac{\boldsymbol{r}_{S/T}}{|\boldsymbol{r}_{S/T}|} \times \hat{\boldsymbol{s}} \tag{27}$$

$$\phi = \cos^{-1}\left(\frac{\boldsymbol{r}_{S/T} \cdot \hat{\boldsymbol{s}}}{|\boldsymbol{r}_{S/T}|\hat{\boldsymbol{s}}}\right) \tag{28}$$

$$\boldsymbol{\beta}_{S/T} = [\cos(\phi/2) \quad \hat{\boldsymbol{e}}\sin(\phi/2)]^T \tag{29}$$

This approach constrains two rotational degrees of freedom for the servicer, but does not constrain the about-boresight rotation. While only representing one degree of freedom, there are significant differences in the torque vector exerted on the target at different servicer attitudes. For an example position with 10 m separation between the spacecraft, rotating the servicer about the line of sight axis results in changes in the total torque magnitude of over 30%. In addition, the direction of the torque vector can change by over 70° by varying servicer orientations at a specific position.

For cases where there is <1% difference in electrostatic torque between different orientations, the servicer attitude is chosen to maximize the distance between the closest points on the two spacecraft in an effort to minimize the probability of a collision between the craft.

Additionally, there are cases where exerting a specific electrostatic torque vector on the target is desirable. These scenarios involve rendezvous with a tumbling target, when electrostatic forces reduce the rotational rate of the target before grappling, or cases where a cooperative client transitions into a free-drift mode before docking and perturbing effects like SRP are negated by electrostatic interactions.

C. Simulation Results

A rendezvous scenario is simulated with a notional GEO spacecraft and servicer, as described in Sec. III. Mass and inertia properties for the target and servicer are taken to be known exactly in the controller and dynamics propagation.

SRP is added as an unmodeled disturbance for the target body, using the nonshadowing model discussed previously. For the GOES-R target, the single asymmetric solar array leads to average SRP induced torques of approximately 0.5 mN · m across all orientations. For comparison, electrostatic torques at 10 m exceed this level when just 1900 V is applied to each spacecraft.

Figure 11 illustrates a straight-line rendezvous perturbed by electrostatic interactions, using a guidance policy that does not account for those electrostatic perturbations. The dashed line illustrates the trajectory unperturbed by electrostatics. Qualitatively, the iterative guidance approach to minimize imparted torques shown in Fig. 12 experiences far less perturbation from the nominal, straight-line trajectory shown in Fig. 11. These simulations are performed with 80 sphere models for the target and 92 spheres for the servicer, and 10 kV potentials on each. This is a severe charging event only relatively infrequently at GEO, but is reasonable to anticipate in a spacecraft lifetime [3]. This scenario therefore offers a plausible instance of significant electrostatic perturbations due to space weather interactions.

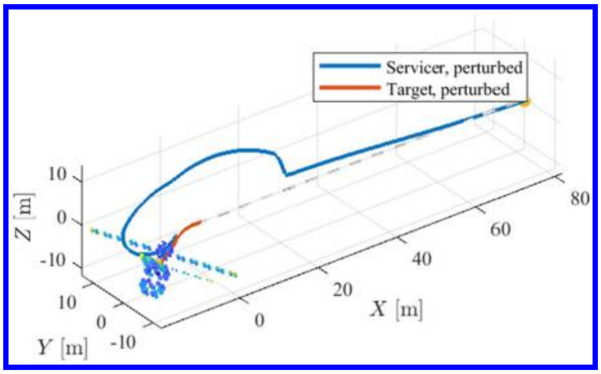

Fig. 11 Rendezvous trajectory perturbed by 10 kV electrostatic potential on each spacecraft, with no guidance accounting for electrostatic interactions.

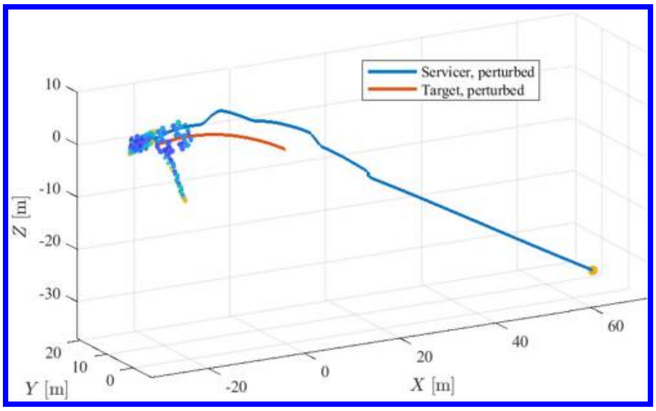

Fig. 12 Rendezvous trajectory perturbed by 10 kV electrostatic potential on each spacecraft, with guidance accounting for electrostatic interactions.

Selecting an approach angle to minimize the electrostatic torque acting on the target during rendezvous results in a greater than 60% decrease in control effort required for rendezvous, and decreases in target rotational rate of over 50%, from 0.025°/s to less than 0.01°/s.

These improvements result in improved docking accuracy, reduced navigation uncertainty, and more predictable lighting conditions. These improvements occur despite not accounting for significant SRP torques in the model. Steady lighting conditions are particularly important in improving optical navigation accuracy during the final meters of rendezvous, when small errors could result in undesired contact between the spacecraft.

For this analysis, both spacecraft are assumed to be at fixed potentials, with electrostatic potentials constant over the entire spacecraft surface. This is in adherence with modern guidelines for spacecraft design, which recommend that all surfaces be continuously conducting and commonly grounded to the spacecraft frame to mitigate arcing hazards. However, this is not an accurate assumption in all cases; older spacecraft were frequently nonconducting, which can result in different components on the structure having potential differences of hundreds or even thousands of volts due to varying material properties and solar photon exposure [8,23]. Inclusion of differential charging effects and the assessment of their impact in proximity operations is an area for future work, and could be augmented by the approach presented in Ref. [39] for incorporating nonconductive structures into an MSM framework.

Given the attitude, position, and approach angle constraints imposed on the servicer, only a limited subset of potential locations are admissible. While the sampling-based method used here may only find a suboptimal local minimum of the electrostatic torque, it is generally within <10% of an absolute minimum torque. This limits the improvements in performance possible through the use of more computationally intensive optimal control strategies. While it is expected that the servicer should be able to determine its own attitude with high precision, uncertainty in target relative pose estimation can drive significant miscalculation of the electrostatic torques between the craft. Taking the gradient of the data shown in Fig. 8 allows the sensitivity of torque to the attitude of the target to be determined. Taking the gradient of torque magnitude in Fig. 8 with respect to angle provides an estimate of the sensitivity of the resultant torque magnitude to target attitude estimation. Some angular regions exhibit sensitivities over 0.03 mN · m/ deg, so just a few degrees of error in target attitude estimates can result in significant errors in computed electrostatic torque.

VI. Optimized Guidance Approach

The sampling-based guidance approach offers significant improvements in final rotational rate; further improvements are obtained by globally optimizing a trajectory to minimize the rate. The sampling-based approach minimizes the net torque parameter at each successive interval, but a superposition of local minima at discrete time steps is not equivalent to a global optimization across the full reference trajectory.

While a wide range of techniques are available for trajectory optimization, a method based on pseudospectral collocation is utilized here. Rather than parameterize the control effort, as is often done in optimal control collocation problems, the target-frame trajectory of the servicer is used. A polynomial function is selected to prescribe the reference trajectory, as it guarantees satisfaction of initial and final position/velocity constraints.

A. Trajectory Parameterization

This trajectory is parameterized in the ${}^{\mathcal{T}}\hat{y}$ and ${}^{\mathcal{T}}\hat{z}$ directions seen in Fig. 5. The ${}^{\mathcal{T}}\hat{x}$ direction follows the nominal reference trajectory in Fig. 5, which preserves the hold points. Additionally, the initial positions and velocities are fixed for all directions, beginning at $[\,80 \quad 0 \quad 0\,]$ m with no initial velocity. The simulation period is fixed at 3.5 h, as in the nominal case. At this final time the trajectory is constrained to reach a position of $[\,1 \quad 0 \quad 0\,]$ m, with no relative velocity.

Additionally, a soft constraint is imposed through a linearly increasing penalty term to ensure that the servicer remains within the approach constraint cone. Smoothly approaching the final state additionally imposes the terminal approach constraint

$$\left.\frac{\mathrm{d}y^*}{\mathrm{d}x^*}\right|_{x^*=0} = \left.\frac{\mathrm{d}z^*}{\mathrm{d}x^*}\right|_{x^*=0} = 0 \tag{30}$$

Differentiating the trajectory prescribing polynomial once provides the velocity at each point in time, while the second derivative provides accelerations. To ensure that the maximum acceleration magnitude is within the control authority bounds set, the second derivative of the position is constrained to fall within the actuation limits.

The hard constraints the optimized trajectory must meet therefore consist of initial position $Y(X(t_o))$, final position $Y(X(t_f))$, initial velocity $\dot{Y}(X(t_o))$, and final velocity $\dot{Y}(X(t_f))$. Because the trajectory is parameterized in the ${}^{\mathcal{T}}y$ and ${}^{\mathcal{T}}z$ directions as a function of the ${}^{\mathcal{T}}x$ reference position x^*, the value of x^* is normalized to improve numerical conditioning for the polynomial trajectory as

$$\chi = \frac{x^*}{x^*(t_o)} \tag{31}$$

This set of initial/final states and rates provides four constraints, so a third-order polynomial with four total terms could fit these constraints perfectly. However, this would provide no variables to tune in the optimization, and consequently could exceed acceleration limits or other imposed constraints. A solution is therefore to use a fifth-order polynomial, as

$$y^*(\chi) = \alpha_1\chi^5 + \alpha_2\chi^4 + \alpha_3\chi^3 + \alpha_4\chi^2 + \alpha_5\chi + \alpha_6 \tag{32}$$

$$z^*(\chi) = \beta_1\chi^5 + \beta_2\chi^4 + \beta_3\chi^3 + \beta_4\chi^2 + \beta_5\chi + \beta_6 \tag{33}$$

where χ is the nondimensional independent variable and α_i represents the coefficients on each term. This formulation for $y^*(\chi)$ and $z^*(\chi)$ provides six total coefficients to determine in $\boldsymbol{\alpha}$ and $\boldsymbol{\beta}$, so a state vector is compiled as

$$\boldsymbol{\kappa}_{y^*} = [\,y_0 \quad y_f \quad \dot{y}_0 \quad \dot{y}_f \quad \ddot{y}_0 \quad \ddot{y}_f\,]^T \tag{34}$$

The acceleration terms $\ddot{y}_0, \ddot{y}_f$ are treated as tuning parameters, and the set of coefficients $\boldsymbol{\alpha}$ is computed to meet these constraints as

$$\boldsymbol{\alpha} = [M]^{-1}\boldsymbol{\kappa}_{y^*} \tag{35}$$

where

$$[M] = \begin{bmatrix} 0 & 0 & 0 & 0 & 0 & 1 \\ 1 & 1 & 1 & 1 & 1 & 1 \\ 0 & 0 & 0 & 0 & 1 & 0 \\ 5 & 4 & 3 & 2 & 1 & 0 \\ 0 & 0 & 0 & 2 & 0 & 0 \\ 20 & 12 & 6 & 2 & 0 & 0 \end{bmatrix} \tag{36}$$

Analogously, the $\boldsymbol{\beta}$ coefficients are computed as

$$\boldsymbol{\beta} = [M]^{-1}\boldsymbol{\kappa}_{z^*} \tag{37}$$

The $[M]$ matrix is equivalent for any fifth-order polynomial and is also used for the z^* and ψ_1^* reference trajectory components.

Therefore, this approach allows the creation of trajectories that meet four constraints precisely, and two bounded parameters that are tuned through the optimization.

Trajectories can be optimized to any number of variables and cost functions, but the primary objective in this case is to minimize the final rotational rate of the target object. A state vector is generated by the optimizer, using the four prescribed and two tuned parameters, and the resultant polynomial coefficient vector $\boldsymbol{\alpha}$ computed. This process is done independently for the ${}^{\mathcal{T}}\hat{y}$, ${}^{\mathcal{T}}\hat{z}$ and $\hat{\psi}_1$ directions. The prescribed trajectory is then used as a reference trajectory input into the reference tracking controller, and the final rotational rate of the target assessed. The optimization is performed to minimize the cost function

$$\mathcal{J} = \boldsymbol{\omega}_f^T\boldsymbol{\omega}_f \tag{38}$$

where $\boldsymbol{\omega}_f^T = \omega_{B/N}(t_f)$ is the angular velocity of the target body at the end of the simulation.

This approach, preserving initial conditions and driving final states/rates to zero, is generalized to a polynomial of arbitrary degree n to describe $y^*(\chi)$ and $z^*(\chi)$ as

$$y^*(\chi) = \alpha_2\chi^2 + \alpha_3\chi^3 + \sum_{j=1}^{n} \alpha_{(j+3)}\chi^{(j+3)} \tag{39}$$

$$z^*(\chi) = \beta_2\chi^2 + \beta_3\chi^3 + \sum_{j=1}^{n} \beta_{(j+3)}\chi^{(j+3)} \tag{40}$$

where the second and third coefficients are related to the initial states for y^* as

$$\begin{bmatrix} \chi_i^2 & \chi_i^3 \\ 2\chi_i & 3\chi_i^2 \end{bmatrix}\begin{bmatrix}\alpha_2\\ \alpha_3\end{bmatrix} = \begin{bmatrix} y_0^* - \sum_{j=1}^{n} \{\alpha_{(i+3)}\chi_i^{(j+3)}\} \\ \frac{V_{y,i}}{V_{x,i}} x_0^* - \sum_{j=1}^{n}\{(j+3)\alpha_{(j+3)}\chi_i^{(j+2)}\}\end{bmatrix} \quad (41)$$

As discussed previously, the servicer attitude is constrained to maintain a line of sight to the target docking port. However this is an underconstrained problem, leaving the servicer attitude free to rotate about the line-of-sight vector. An additional polynomial is used to prescribe the rotation about this vector as a function of the X position, developed analogously to the trajectories in $\hat{y}$, $\hat{z}$ as

$$\psi_1(\chi) = \gamma_1\chi^5 + \gamma_2\chi^4 + \gamma_3\chi^3 + \gamma_4\chi^2 + \gamma_5\chi + \gamma_6 \quad (42)$$

A quintic polynomial is found to perform well in prescribing both translation and rotational positions, with little improvement offered by higher-order polynomials for this rendezvous scenario. Higher orders allow better fitting and more optimal solutions in cases with initially rotating target bodies, however.

Final rotational rate is strongly dependent on the inertia properties of the target vehicle, so a proxy measure of minimizing the torque imparted on the target over the rendezvous trajectory is preferable if the center-of-mass location is more accurately known. Torque acting on the uncooperative target for this scenario is only a function of spacecraft relative pose and target center-of-mass location, sun angle, and electrostatic potentials, decreasing the target parameters that need to be determined.

The inertia and mass properties are likely to be the most poorly defined aspect of the target, as spacecraft at end of life typically have some (uncertain) quantity of residual fuel remaining. Additionally, in a servicing or debris remediation mission where the spacecraft may have broken up to some extent, a priori knowledge of the inertia properties is highly uncertain [29].

Optimization of this trajectory is performed using MATLAB's *fminsearch* unconstrained optimization function. This method results in a final target rotational rate of just 0.006° when subject to 10 kV potential levels and SRP. The initial trajecotry and attitudes are shown in Fig. 13, while the final result from following this trajectory with electrostatic and SRP perturbations is shown in Fig. 14.

These results present a significant improvement in final rotational rate over the sampling-based algorithm, but at dramatically increased computational cost. While the sampling-based approach could compute a desired approach vector and attitude in ~0.1 s, the *fminsearch* optimizer required ~10^4 times longer and thousands of iterations to converge, with each requiring integration for a full trajectory. Such high computation times occurred despite having just six total tuning parameters. Increasing the search space with higher-fidelity polynomials comes with an accompanying increase in computational time. Therefore, although the sampling approach provides a suboptimal solution to the trajectory, it has benefits in computational burden, enabling on-orbit recomputation as potential estimates evolve.

Figure 15 illustrates the impact of different potential levels on the optimized approach trajectory. Similar final rotational rates are achieved by both trajectories, but there significant differences are notable in the two optimized trajectory components.

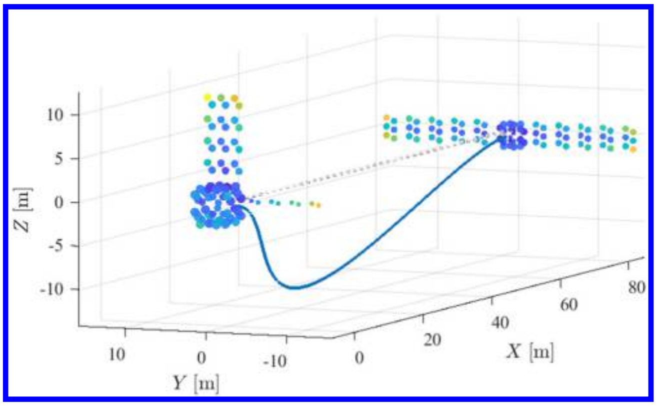

Fig. 13 Precomputed optimal trajectory, initial states.

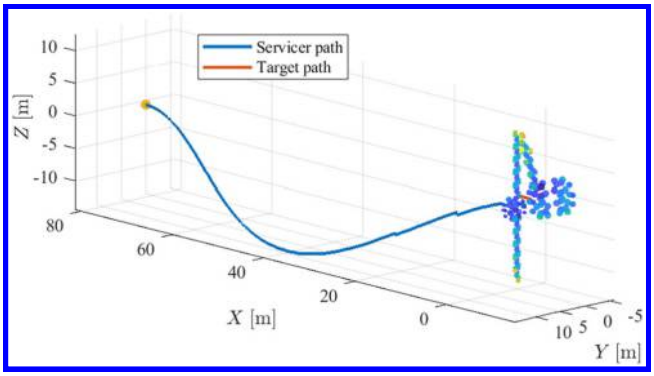

Fig. 14 Precomputed optimal trajectory, final result.

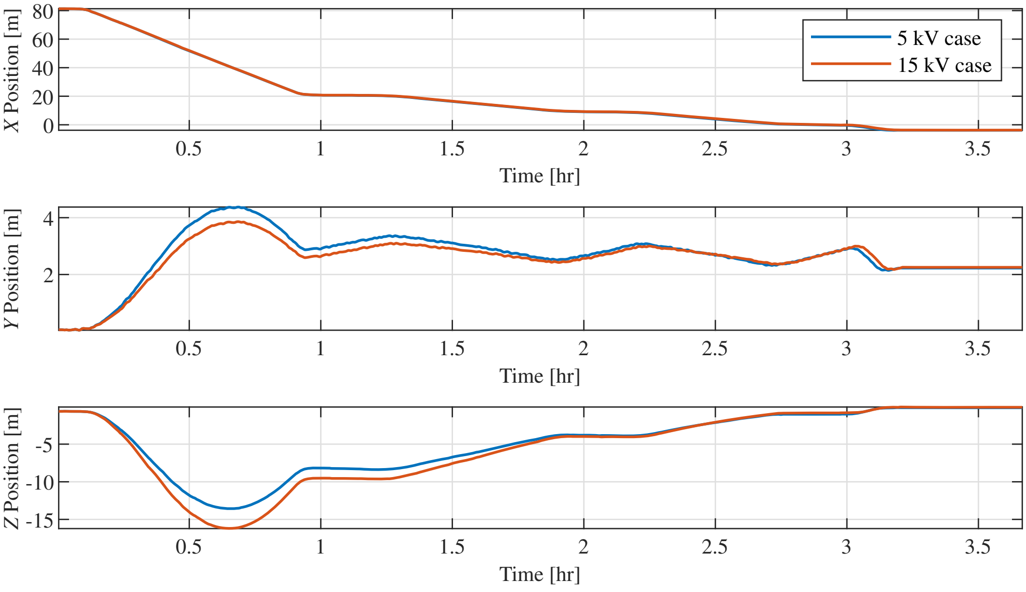

Fig. 15 Optimized trajectories for 5 and 15 kV cases.

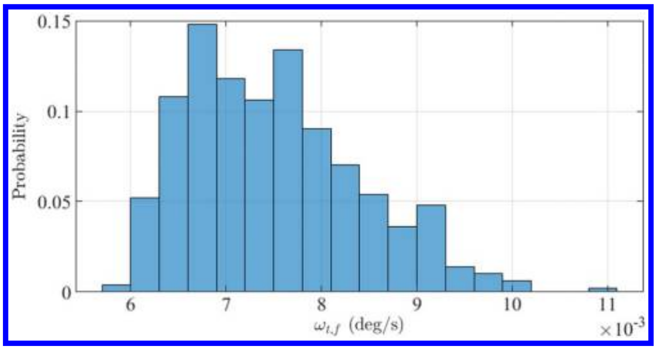

Fig. 16 Target final rotational rate through 500 runs of a Monte Carlo simulation.

B. Monte Carlo Simulation

The polynomial-based guidance approach shows an order-of-magnitude improvement over the deterministic sampling-based approach, but has disadvantages in computation time that likely limit it to ground-side path planning. Therefore, it is important that this approach be robust to varying scenario parameters. A Monte Carlo simulation is conducted to evaluate performance under mismodeled parameters. The same optimized trajectory was evaluated for 500 simulations. Inertia properties are evaluated with 5% 1σ normally distributed variation in each element. Additionally, linearly time-varying spacecraft potentials are imposed for the target to represent the space environment evolution, ranging from the nominal 10 ± 0.1 kV, 1 standard deviation at the beginning of the simulation, to 10 ± 1 kV, 1 standard deviation at the end.

The results of this analysis, seen in Fig. 16, show that the designed trajectory is robust to uncertainties in potential and inertia properties. Therefore it is reasonable to precompute a trajectory from the initial 80 m hold point based on observations of relative potential, and follow that trajectory. The worst result in this assessment was $0.011°/\mathrm{s}$, which is approximately twice the optimized rate. However, this result is still approximately equal to the solution computed through the deterministic sampling-based approach.

VII. Conclusions

While electrostatic perturbations significantly impact proximity operations dynamics, it is possible to use new methods to remotely sense the potential on an object in tandem with rapid techniques for evaluating the resultant intercraft forces and torques to mitigate these concerns. A computationally efficient solution to guidance during final approach can reduce the impact of electrostatic interactions by over 50%. Moreover, this strategy can be applied in combination with various constraints on attitude or position during approach. In comparison, a trajectory globally optimized to reduce the rotational rate of the target at grappling reduces the rotational rate of the target by 95% relative to a naive approach that does not account for electrostatics. However, this approach is computationally expensive and would be very difficult to implement in a flight processor, instead requiring precomputation offline.

Acknowledgment

This work was supported through Air Force Office of Scientific Research grant #FA9550-20-1-0025.

References

[1] Wilson, K., and Schaub, H., “Impact of Electrostatic Perturbations on Proximity Operations in High Earth Orbits,” *AAS/AIAA Astrodynamics Specialist Conference*, 2020.

[2] Wilson, K., and Schaub, H., “Impact of1Electrostatic Perturbations on Proximity Operations in High-Earth Orbits,” *Journal of Spacecraft and Rockets*, 2021.
https://doi.org/10.2514/1.A35039

[3] Olsen, R. C., “Record Charging Events from Applied Technology Satellite 6,” *Journal of Spacecraft and Rockets*, Vol. 24, No. 4, 1987, pp. 362–366.
https://doi.org/10.2514/3.25925

[4] Hogan, E., and Schaub, H., “Relative Motion Control for Two-Spacecraft Electrostatic Orbit Corrections,” *AIAA Journal of Guidance, Control, and Dynamics*, Vol. 36, No. 1, 2013, pp. 240–249.
https://doi.org/10.2514/1.56118

[5] Hughes, J. A., and Schaub, H., “Heterogeneous Surface Multisphere Models Using Method of Moments Foundations,” *Journal of Spacecraft and Rockets*, Vol. 56, No. 4, 2019, pp. 1259–1266.
https://doi.org/10.2514/1.A34434

[6] Wilson, K. T., Bengtson, M., and Schaub, H., “Hybrid Method of Remote Sensing of Electrostatic Potential for Proximity Operations,” *IEEE Aerospace Engineering Conference*, 2020.

[7] Matéo-Vélez, J.-C., Sicard, A., Payan, D., Ganushkina, N., Meredith, N. P., and Sillanpäa, I., “Spacecraft Surface Charging Induced by Severe Environments at Geosynchronous Orbit,” *Space Weather*, Vol. 16, No. 1, 2018, pp. 89–106.
https://doi.org/10.1002/2017SW001689

[8] Olsen, R. C., McIlwain, C. E., and Whipple, E. C., Jr., “Observations of Differential Charging Effects on ATS 6,” *Journal of Geophysical Research: Space Physics*, Vol. 86, No. A8, 1981, pp. 6809–6819.
https://doi.org/10.1029/JA086iA08p06809

[9] “NASA-HDBK-4006A: Low Earth Orbit Spacecraft Charging Design Handbook,” NASA Office of the Chief Engineer, 2018, https://standards.nasa.gov/standard/nasa/nasa-hdbk-4006.

[10] “NASA-HDBK-4002A: Mitigating In-Space Charging Effects—A Guideline,” NASA Office of the Chief Engineer, 2011, https://standards.nasa.gov/standard/nasa/nasa-hdbk-4002.

[11] Dennison, J. R., “Dynamic Interplay Between Spacecraft Charging, Space Environment Interactions, and Evolving Materials,” *IEEE Transactions on Plasma Science*, Vol. 43, No. 9, 2015, pp. 2933–2940.
https://doi.org/10.1109/TPS.2015.2434947

[12] Mateo-Velez, J.-C., Belhaj, M., Dadouch, S., Sarrailh, P., Hess, S. L. G., and Payan, D., “Spacecraft Worst Case Surface Charging: On the Importance of Measuring the Electron Emission Yield Under Representative Environmental Conditions,” *IEEE Transactions on Plasma Science*, Vol. 47, No. 8, 2019, pp. 3790–3795.
https://doi.org/10.1109/TPS.2019.2925435

[13] Ferguson, D. C., and Holeman, E., “Arcing on GEO Satellites in the Arecibo Sidelobes,” *AIAA Scitech 2022 Forum*, AIAA Paper 2022-1991, 2022.
https://doi.org/10.2514/6.2022-1991

[14] Ozkul, A., Lopatin, A., Shipp, A., Pitchford, D., Mazur, J. E., and Roeder, J. L., et al., “Initial Correlation Results of Charge Sensor Data from Six Intelsat VIII Class Satellites with Other Space and Ground Based Measurements,” edited by R. A. Harris, Vol. 476, Spacecraft Charging Technology, ESA Special Publication, ESA, Noordwijk, The Netherlands, 2001, p. 293.

[15] Wilson, K., “Remote Electrostatic Potential Determination for Spacecraft Relative Motion Control,” Ph.D. Thesis, Univ. of Colorado Boulder, Boulder, CO, 2021.

[16] Koons, H., Mazur, J., Lopatin, A., Pitchford, D., Bogorad, A., and Herschitz, R., “Spatial and Temporal Correlation of Spacecraft Surface Charging in Geosynchronous Orbit,” *Journal of Spacecraft and Rockets*, Vol. 43, No. 1, 2006.
https://doi.org/10.2514/1.10805

[17] Cho, M., Kawakita, S., Nakamura, M., Takahashi, M., Sato, T., and Nozaki, Y., “Number of Arcs Estimated on Solar Array of a Geostationary Satellite,” *Journal of Spacecraft and Rockets*, Vol. 42, No. 4, 2005, pp. 740–748.
https://doi.org/10.2514/1.6694

[18] Stevenson, D., and Schaub, H., “Multi-Sphere Method for Modeling Electrostatic Forces and Torques,” *Advances in Space Research*, Vol. 51, No. 1, 2013, pp. 10–20.
https://doi.org/10.1016/j.asr.2012.08.014.

[19] Stevenson, D., and Schaub, H., “Multi Sphere Modeling for Electrostatic Forces on Three-Dimensional Spacecraft Shapes,” *AAS/AIAA Spaceflight Mechanics Meeting*, 2012.

[20] Maxwell, J., Wilson, K., Hughes, J., and Schaub, H., “Multisphere Method for Flexible Conducting Space Objects: Modeling and Experiments,” *Journal of Spacecraft and Rockets*, Vol. 57, No. 2, 2020, pp. 225–234.
https://doi.org/10.2514/1.A34560

[21] Lundgreen, P., and Dennison, J., “Strategies for Determining Electron Yield Material Parameters for Spacecraft Charge Modeling,” *Space Weather*, Vol. 18, No. 4, 2020.
https://doi.org/10.1029/2019SW002346

[22] Mozer, F. S., “DC and Low-Frequency Double Probe Electric Field Measurements in Space,” *Journal of Geophysical Research: Space*

Physics, Vol. 71, No. 11, 2016, pp. 10,942–10,953.
https://doi.org/10.1029/JZ071i011p02701

[23] Sarno-Smith, L. K., Larsen, B. A., Skoug, R. M., Liemohn, M. W., Breneman, A., Wygant, J. R., and Thomsen, M. F., “Spacecraft Surface Charging Within Geosynchronous Orbit Observed by the Van Allen Probes,” *Space Weather*, Vol. 14, No. 2, 2016, pp. 151–164.
https://doi.org/10.1002/2015SW001345

[24] Wilson, K., and Schaub, H., “Environmental X-ray Considerations for Bremsstrahlung-Based Surface Potential Determination,” *AIAA SciTech*, AIAA, Reston, VA, 2020.

[25] Bengtson, M., Hughes, J., and Schaub, H., “Prospects and Challenges for Touchless Sensing of Spacecraft Electrostatic Potential Using Electrons,” *IEEE Transactions on Plasma Science*, Inst. of Electrical and Electronics Engineers, New York, 2019.

[26] Lai, S. T., *Fundamentals of Spacecraft Charging: Spacecraft Interactions with Space Plasmas*, Princeton Univ. Press, Princeton, NJ, 2011.

[27] Perfetto, D. M., Opromolla, R., Grassi, M., and Schmitt, C., “LIDAR-Based Model Reconstruction for Spacecraft Pose Determination,” *2019 IEEE 5th International Workshop on Metrology for AeroSpace (MetroAeroSpace)*, Inst. of Electrical and Electronics Engineers, New York, 2019, pp. 1–6.
https://doi.org/10.1109/MetroAeroSpace.2019.8869585

[28] Opromolla, R., Fasano, G., Rufino, G., and Grassi, M., “Uncooperative Pose Estimation with a LIDAR-Based System,” *Acta Astronautica*, Vol. 110, May–June 2015, pp. 287–297.
https://doi.org/10.1016/j.actaastro.2014.11.003

[29] Ivanov, D., Ovchinnikov, M., and Sakovich, M., “Relative Pose and Inertia Determination of Unknown Satellite Using Monocular Vision,” *International Journal of Aerospace Engineering*, 2018.
https://doi.org/10.1155/2018/9731512

[30] Borovsky, J. E., and Denton, M. H., “Magnetic Field at Geosynchronous Orbit During High-Speed Stream-Driven Storms: Connections to the Solar Wind, the Plasma Sheet, and the Outer Electron Radiation Belt,” *Journal of Geophysical Research: Space Physics*, Vol. 115, No. A8, 2010.
https://doi.org/10.1029/2009 JA015116

[31] Baumjohann, W., and Treumann, R. A., *Basic Space Plasma Physics*, Imperial College Press, London, 1996.
https://doi.org/10.1142/p015

[32] Hartley, D. P., Denton, M. H., and Rodriguez, J. V., “Electron Number Density, Temperature, and Energy Density at GEO and Links to the Solar Wind: A Simple Predictive Capability,” *Journal of Geophysical Research: Space Physics*, Vol. 119, No. 6, 2014, pp. 4556–4571.
https://doi.org/10.1002/2014 JA019779

[33] Spiridonova, S., and Kahle, R., “Relative Orbit Dynamics in Near-Geostationary Orbits,” *International Symposium on Space Flight Dynamics*, 2015.

[34] List, M., Bremer, S., Benny, R., and Selig, H., “Modelling of Solar Radiation Pressure Effects: Parameter Analysis for the MICROSCOPE Mission,” *International Journal of Aerospace Engineering*, 2015.
https://doi.org/10.1155/2015/928206

[35] Schaub, H., and Junkins, J. L., *Analytical Mechanics of Space Systems*, 4th ed., AIAA Education Series, AIAA, Reston, VA, 2019.

[36] Marshall, T., and Fletcher, M., “Meeting High-Qualitiy RWA Commercial Demand Through Innovative Design,” *Space Mechanisms and Tribology, Proceedings of the 8th European Symposium*, 1999.

[37] Luo, Y., Zhang, J., and Tang, G., “Survey of Orbital Dynamics and Control of Space Rendezvous,” *Chinese Journal of Aeronautics*, Vol. 27, No. 1, 2014, pp. 1–11.
https://doi.org/10.1016/j.cja.2013.07.042

[38] Mazur, J. E., Fennell, J. F., Roeder, J. L., O’Brien, P. T., Guild, T. B., and Likar, J. J., “The Timescale of Surface-Charging Events,” *IEEE Transactions on Plasma Science*, Vol. 40, No. 2, 2012, pp. 237–245.
https://doi.org/10.1109/TPS.2011.2174656

[39] Hughes, J., and Schaub, H., “Guidance, Navigation and Control Advances in Electrostatic Attitude Control on Passive GEO Objects,” *9th International Workshop on Satellite Constellations and Formation Flying*, 2017, Paper IWSCFF 17-16.

J. Reuther
Associate Editor